

Raman spectroscopy of holey nanographene C216

Ali Maghsoumi¹ | Uliana Beser² | Xinliang Feng^{3,4} | Akimitsu Narita² | Klaus Müllen² | Chiara Castiglioni¹ | Matteo Tommasini¹

¹Dipartimento di Chimica, Materiali e Ingegneria Chimica, Politecnico di Milano, Milan, Italy

²Max Planck Institute for Polymer Research, Mainz, Germany

³Center for Advancing Electronics Dresden (CFAED) and Department of Chemistry and Food Chemistry, Dresden University of Technology, Dresden, Germany

⁴Max Planck Institute of Microstructure Physics, Halle (Saale), Germany

Correspondence

Chiara Castiglioni, Dipartimento di Chimica, Materiali e Ingegneria Chimica, Politecnico di Milano, Piazza Leonardo da Vinci 32, 20133 Milan, Italy.
Email: chiara.castiglioni@polimi.it

Funding information

Italian Ministry of Education, Universities and Research (MIUR), Grant/Award Number: 2017PJ5XXX; Max Planck Society

Abstract

We report a detailed investigation by Raman spectroscopy of the holey nanographene **C216**, a hexagon-shaped disk with armchair edges (1.4 nm long), from which the central aromatic ring is missing. Density functional theory (DFT) calculations allow to assign the main features of the Raman spectra that have been recorded with several excitation wavelengths. In the Raman spectra, we observe signatures of the hole in the structure, several G and D modes, as well as their overtones and combinations—up to third order.

KEYWORDS

DFT modeling, G and D overtones and combinations, graphene molecules, multi-wavelength Raman, polycyclic aromatic hydrocarbons

1 | INTRODUCTION

Polycyclic aromatic hydrocarbons (PAHs) have played an important role for the development of modern organic chemistry from a synthetic, spectroscopic, and theoretical point of view.^[1–10] They have also served as active components of (opto)electronic devices.^[11–13] The versatile design features for PAHs include mode of fusion of benzene rings, edge type, heteroatom incorporation, and substitution.^[14–16]

In recent decades, PAH research has seen a major renaissance, partly, stimulated by the rise of graphene as 2-D material and by the development of single-molecule

electronics.^[1,17,18] Of particular value, thereby, is the perfect control of electronic characteristics by molecular design^[19–25] that also rules supramolecular properties such as packing in the solid state or the formation of mesophases.^[26–29] The size of PAHs has been increased toward the nanoscale, and the so-called nanographenes (NGs) have shown immense value as molecularly defined models of graphene.^[30,31] Typical examples are hexagon-shaped hexa-*peri*-hexabenzocoronene (**HBC**) and C₂₂₂H₄₂, or so-called **C222**, with 222 sp² carbons in its aromatic core.^[19,32] When overlooking these impressively large, but nevertheless atomically precise, disk structures, a good case can be made by relating their electronic and

This is an open access article under the terms of the [Creative Commons Attribution-NonCommercial-NoDerivs](https://creativecommons.org/licenses/by-nc-nd/4.0/) License, which permits use and distribution in any medium, provided the original work is properly cited, the use is non-commercial and no modifications or adaptations are made.

© 2021 The Authors. *Journal of Raman Spectroscopy* published by John Wiley & Sons Ltd.

vibrational properties to their geometrical confinements with respect to graphene.^[33–35] Further, extending NGs into one direction has furnished graphene nanoribbons (GNRs) as a new family of conjugated polymers.^[30,36–39] Like graphene, GNRs exhibit exciting electronic properties, but unlike graphene, they possess a non-vanishing band gap, which qualifies them, in particular, as valuable semiconductors for developing field effect transistors.

The above graphene-related structures are often sparingly soluble in organic solvents, which hampers not only their processability upon device fabrication but also their detailed structure proof by nuclear magnetic resonance (NMR) or single-crystal X-ray analysis. These characteristics make vibrational spectroscopy an especially valuable tool for studying such NGs and GNRs in the solid state or as thin films. Notably, because of resonance effects and of the strong coupling of π - π^* excitations with peculiar collective CC stretching vibrations,^[33] Raman spectroscopy of graphene-related structures has provided many significant markers of molecular structure that proved the success of the synthesis in guaranteeing a perfect structure control.^[40–46]

The vibrational states of NGs are strongly correlated with the phonons of graphene: the Raman transitions of NGs associated to collective CC stretching modes find a counterpart in the Raman peaks of graphene.^[33–35,47] Interestingly, the wavenumber and the intensity of the strong Raman bands of NGs depend on the confinement of the π electrons due to the finite size of the molecule and provide fingerprints of the molecular point group symmetry.^[48] In addition, modes involving edges and/or atoms/functional groups on the borders are sensitive to the peculiar edge topology and chemistry, as is exemplified by the case of the CH out-of-plane bending modes.^[49,50]

With the exception of localized group modes associated to functional groups possibly decorating the borders of the NGs, the strong and characteristic Raman active modes involve the network of condensed aromatic rings that constitute the NGs and provide markers of the NGs as a whole. Therefore, only the detailed analysis of the nuclear displacements associated with the Raman transitions, computed by the available quantum chemistry approaches (notably, density functional theory, DFT), can provide specific Raman markers (peaks and relative intensities) of the chemical structures featured by a given NG. This is the main reason that the study of the Raman spectra of NGs cannot be limited to empirical correlation analysis of the experimental spectra, which are typical of analytical spectroscopy and work very well in presence of normal modes localized on specific functional groups.

Finally, the Raman spectra of NGs can be recorded noninvasively on the as-obtained materials, on

concentrated solutions, or films ready for use in devices. One may thus also obtain valuable insights into intermolecular interactions in aggregates and in solid phases of interest for the applications of NGs.

By following the approach sketched above, this paper highlights the wealth of information that can be obtained by Raman spectroscopy and DFT calculations, considering the intriguing case of the **C216** coronoid NG (Figure 1). There is a further motivation from the side of materials science. Cycloarenes and coronoids,^[51,52] namely, PAHs with cyclic structures featuring a cavity as kekulene,^[53] have been revisited,^[54–61] serving as model structures of graphene nanomesh (GNM). GNM comprises graphene sheets with pores, where the size and the size distribution of the pores can modulate the electronic structure and also determine the behavior as membrane material.^[62–67] We have recently reported a synthesis of $C_{216}H_{48}$ (**C216**), as the coronoid analogue of **C222**, with the missing central ring (hole), which demonstrated the increase of the energy gap upon introduction of the hole^[68] (see Figure 1). More recently, Liu et al. reported a theoretical study on **C216**, displaying its potential as ideal membrane for hydrogen purification.^[69] As discussed below, Raman spectroscopy and DFT calculations are used here as a probe of the specific molecular structure of **C216**: indeed, they provide signatures of the presence of the “hole.” Altogether, the detailed analysis of defined model compounds is intended to highlight Raman spectroscopy as an indispensable tool for the characterization of graphenes and related materials.

2 | STRUCTURE OF C216

We show here that the occurrence of a hole in **C216** may affect the planarity of the molecule. Although this out-of-plane distortion is not expected to significantly lower π conjugation (similar to other distorted PAHs—see, for instance, Maghsoumi et al.^[40]), the presence of a hole in **C216** significantly affects the conjugation pattern and modifies the HOMO-LUMO gap.

The molecular structure of **C216** was recently discussed in the general context of kekulenes,^[51] a family of cyclic arenes. The hole edge in **C216** is capped with hydrogen atoms that are close enough to exert some steric hindrance, which is responsible of the nonplanar structure. The instability of the planar versus the nonplanar structure in a holey PAH can be straightforwardly investigated by geometry optimization and calculation of vibrational frequencies. For sake of simplicity, we investigated in detail such instability considering **C108**, a smaller analogue of **C216** (Figure 2). The occurrence of a sizable imaginary wavenumber ($120i\text{ cm}^{-1}$) in planar

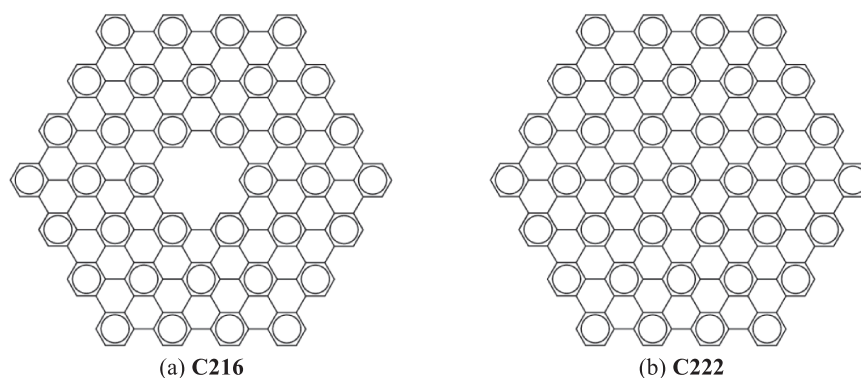


FIGURE 1 Molecular structure of **C216** (left), the analogue of the **C222** (right) nanographene (NG) with the missing central ring (hole). The structures are sketched following the Clar's^[70] rule: accordingly, aromatic "Clar rings" (with a circle inside) are linked by longer CC bonds. The occurrence of two different kinds of CC bonds in polycyclic aromatic hydrocarbons (PAHs) has been shown by theoretical models, through geometry optimization^[33] and the related electronic structure was proven by Scanning Tunneling Microscopy (STM) investigations.^[25] The network of CC bonds in PAHs can be regarded as a slightly relaxed geometry starting from a graphene-like structure characterized by perfectly equalized CC bonds

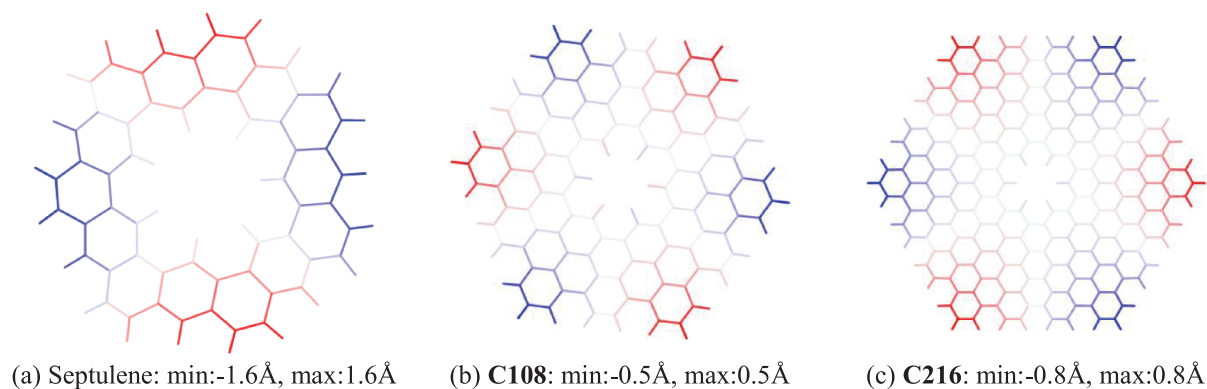


FIGURE 2 Schematic representation of the nonplanar structure of **C216** (D_{3d} symmetry point group) compared with that of septulene and of **C108** (D_{3d} symmetry), the smaller analogue of **C216**, ideally obtained from the giant polycyclic aromatic hydrocarbon (PAH) **C114** (D_{6h} symmetry) by removal of the inner ring. The molecules are represented by means of an orthogonal projection (projection on the mirror plane involved in the S_6 symmetry operation). The out-of-plane z coordinate of the middle point of each bond is coded in shades of red ($z > 0$) and blue ($z < 0$). In-plane bonds are coded with light gray shade. Molecular structures have been obtained from geometry optimization with density functional theory (DFT) method B3LYP/6-31G(d,p). For the structures illustrated, the diagonalization of the Hessian does not give any imaginary wavenumber, thus confirming that they are stable structures. The six rings on the vertexes of **C216** (and **C108**) adopt an alternated up-down conformation. This structure can be schematically labeled (ududud) by following a path along the periphery of the molecule

C108 indicates that such flat geometry corresponds to a saddle point of the intramolecular potential energy surface. As expected, the vibrational eigenvector associated to the imaginary wavenumber describes nuclear displacements involving alternated out-of-plane CH bending at the hole edge.

By relaxing planarity in the guess geometry adopted to start optimization, the **C108** molecule escapes from the saddle point and reaches a stable nonplanar minimum, in correspondence of which no imaginary frequencies are found anymore. With respect to the saddle point, this

minimum is more stable by only 0.16 kcal/mol; however, despite the small energy difference, the wavenumber of the collective in phase CH out-of-plane bending (a very characteristic infrared (IR) marker of the hole, see Figure 3), is affected by the break of planarity. This marker is computed at 873 cm^{-1} in the planar case, while it shifts at 886 cm^{-1} in the nonplanar case, showing a remarkable blue shift of 13 cm^{-1} .

Similar to **C108**, the steric hindrance at the hole edges also drives out-of-planarity **C216**: the molecule takes a shape where the six vertexes are alternatively pointing up

or down with respect to the average molecular plane (*ududud* shape—see Figure 2). Hence, even if steric hindrance is not as severe as in the perchlorinated case of **HBC-Cl** (see Maghsoumi et al.^[40]), also **C216** adopts a slightly bent nonplanar structure, at least in the gas phase limit (see Figure 4). This molecular structure belongs to the D_{3d} symmetry point group.

3 | RAMAN SPECTROSCOPY OF C216

PAHs molecules show characteristic Raman spectra whose common features arise from the honeycomb network of condensed aromatic rings. Because of the high polarizability of π electrons, some vibrational modes that involve the collective stretching of the CC bonds of these rings show very strong Raman bands. The analysis of the normal modes allows to establish a connection between such strongly Raman active modes of NGs and the phonons of graphene, following to the so-called *oligomer approach*.^[33–35,71] Moreover, the study of the Raman

spectra of several PAHs with different size, symmetry, and edge topology clearly proved that such structural variety affects the Raman spectra, most notably in the D region.^[34,35,48] Therefore, the analysis of the Raman spectra of NGs has provided evidence of their structures in several circumstances.^[41,42,44,50,72]

The Raman spectra of **C216** and **C222** have been recorded with different laser lines (325, 458, 488, 514, 633, and 785 nm—see Figure 5). As expected, all the Raman spectra display the characteristic features of NGs, that is, the occurrence of structured bands in the same regions where the G and D lines of graphene are observed. These Raman fingerprints of graphene/graphite (in the first-order spectrum) are assigned to the phonons sketched in Figure 6.

Before discussing in detail the Raman spectra of **C216**, it is worth mentioning that the comparison of experimental data with simulations of the Raman spectra based on pre-resonance DFT calculations will show some discrepancies in the pattern of relative intensities. These shortcomings can originate from several issues. The theoretical description of the energies of relevant

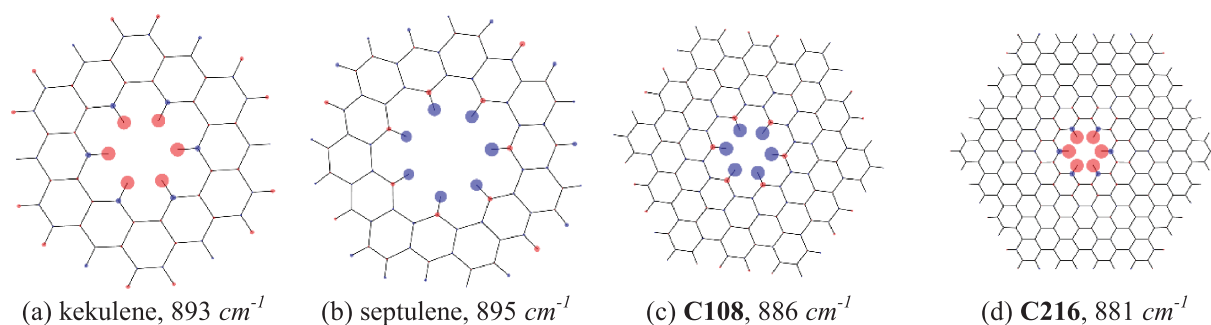


FIGURE 3 CH-out-of-plane nuclear displacements (from vibrational eigenvectors) associated to the infrared (IR) markers of the hole topology in annular polycyclic aromatic hydrocarbons (PAHs) according to density functional theory (DFT) calculations. Red (or blue) circles indicate atoms, which are displaced out-of-plane during the vibrational mode; the radius of the circle is proportional to the atom displacement

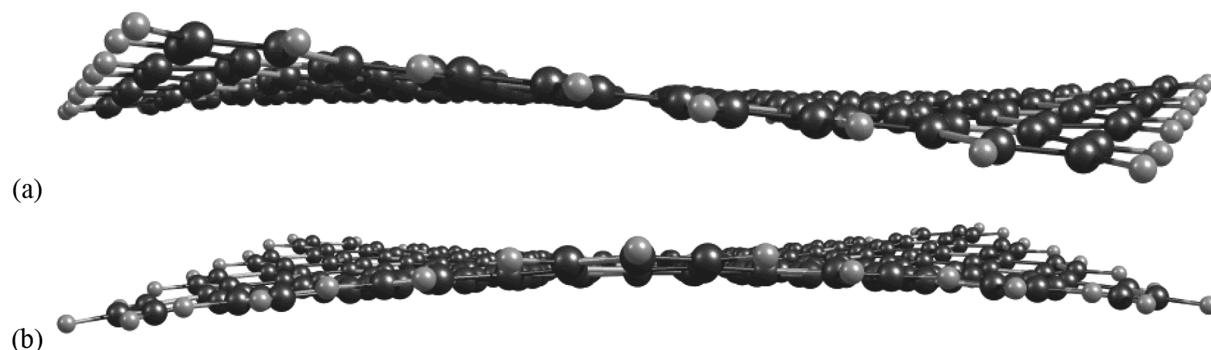


FIGURE 4 Side view of the **C216** structure obtained from geometry optimization by density functional theory (DFT) methods (see Section 5 for details). (b) has been rotated by 60° compared to (a)

FIGURE 5 Comparison between experimental Raman spectra of **C216** and **C222** recorded with different laser wavelengths (top panel) and simulated Raman spectra based on density functional theory (DFT) calculations of the Raman cross section carried out for selected excitation wavelengths (bottom panel)

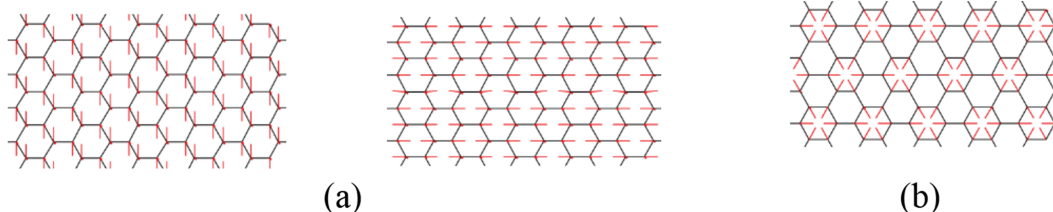
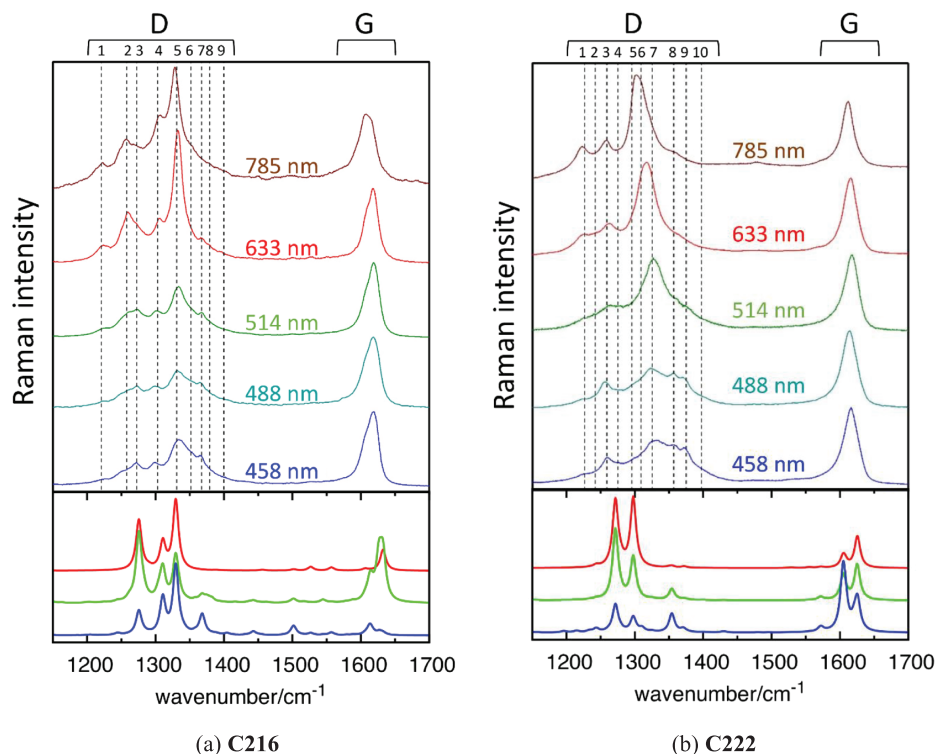


FIGURE 6 Sketch of the graphene phonons associated to the first-order Raman features of graphene. (a) E_{2g} phonon (Γ point, first BZ), responsible of the G line. (b) A_1 phonon (K point, first BZ); its nuclear displacements correlate with the vibrational pattern of the phonons at \mathbf{q} wave vector close to \mathbf{K} that are responsible for the D line. These phonons describe a collective breathing of the rings and correspond to forbidden Raman transitions for a perfect graphene sheet, which become strongly active by the occurrence of structural disorder^[73,74]

electronic excited states could not reproduce with the needed accuracy the real situation, because of intrinsic limitations of DFT and because experiments are carried out on solid-state samples, while calculations model isolated species. These limitations in the description of the electronic structure affect the computed Raman intensities at a given excitation energy, thus describing resonance or pre-resonance phenomena in a way which does not match exactly the experimental situation. For the sake of simplicity, and because time-dependent DFT (TD-DFT) excitation energies are close enough to the broad absorption band measured for **C216**,^[68] we decided to compute Raman intensities at the same excitation wavelength values used in our experiments. This simple computational strategy allows to account for the observed

trends and provides us with the suitable tools for the vibrational assignment and interpretation of the most relevant spectral features. Other approaches are available for the accurate calculation of resonance Raman intensities through the evaluation of Franck–Condon factors.^[75,76] However, given the large size of the investigated molecules, they are presently deemed too expensive from the computational point of view.

To ease the analysis of the Raman spectra, in the following discussion, we will consider separately three spectral ranges, namely, (a) the medium wavenumber region featuring the D and G bands ($1000\text{--}1800\text{ cm}^{-1}$), (b) the low-wavenumber region ($<1000\text{ cm}^{-1}$), and (c) the high-wavenumber region comprising overtone and combination bands ($>1800\text{ cm}^{-1}$). The spectra of **C216** and **C222**

will be presented and discussed in a comparative way, in order to highlight common features, and spectroscopic markers specifically related to the presence of the hole.

3.1 | Medium wavenumber region (1000–1800 cm^{-1})

As reported in Figure 5, the experimental Raman spectra of **C216** and **C222** excited with several laser lines show a very broad and structured D band (1150–1450 cm^{-1}). It displays in both molecules several peaks and shoulders. It is also evident that the Raman spectra in this region are sensitive to the excitation energy. A good fit of the D band requires at least 9 different Lorentzian components (D_1 – D_9) for **C216** and 10 components (D_1 – D_{10}) for **C222**. In both molecules, the relative intensities are sensitive to the excitation wavelength. We report in Tables 1 and 2 the positions of the D_i peaks for **C216** and **C222**, as obtained from the deconvolution of the experimental spectra. Because each D_i component should be assigned to a specific molecular normal mode, its wavenumber is expected to be independent with respect to the laser excitation, at least within experimental error and considering some uncertainty related to the band deconvolution procedure. Indeed, this can be checked by inspection of the data reported in Tables 1 and 2, which proves the soundness of the deconvolution procedure.

We report in Tables 3 and 4 the results of a detailed analysis of the Raman activities and wavenumbers computed by DFT for **C216** and **C222**. We settled the correspondence between Raman transitions predicted by calculations and the experimentally observed D_i components by considering the Raman activities determined by DFT together with the associated wavenumbers. We focused on DFT calculations carried out with

TABLE 1 Position of the main components of the Raman signal in the D region of **C216** as a function of the laser excitation (from band deconvolution)

| | 458 nm | 488 nm | 514 nm | 633 nm | 785 nm |
|-------|--------|--------|--------|--------|--------|
| D_1 | 1219 | 1219 | 1221 | 1221 | 1218 |
| D_2 | 1250 | 1254 | 1254 | 1256 | 1252 |
| D_3 | 1269 | 1271 | 1271 | 1272 | 1269 |
| D_4 | 1295 | 1295 | 1298 | 1302 | 1302 |
| D_5 | 1329 | 1328 | 1329 | 1329 | 1325 |
| D_6 | 1348 | 1348 | 1349 | 1348 | 1348 |
| D_7 | 1363 | 1362 | 1364 | 1364 | 1365 |
| D_8 | 1375 | 1376 | 1375 | 1374 | 1374 |
| D_9 | 1395 | 1398 | 1395 | 1390 | 1389 |

TABLE 2 Position of the main components of the Raman signal in the D region of **C222** as a function of the laser excitation (from band deconvolution)

| | 458 nm | 488 nm | 514 nm | 633 nm | 785 nm |
|----------|--------|--------|--------|--------|--------|
| D_1 | 1226 | 1222 | 1225 | 1222 | 1221 |
| D_2 | | | | 1240 | 1244 |
| D_3 | 1257 | 1254 | 1261 | 1259 | 1256 |
| D_4 | 1273 | 1272 | | | 1273 |
| D_5 | 1293 | 1293 | 1292 | | 1296 |
| D_6 | | | 1306 | 1311 | 1304 |
| D_7 | 1326 | 1322 | 1324 | 1320 | 1320 |
| D_8 | 1353 | 1353 | 1357 | 1356 | 1351 |
| D_9 | 1371 | 1369 | 1375 | | |
| D_{10} | 1393 | 1393 | 1397 | | |

$\lambda_{\text{exc}} = 514$ nm. Among the many vibrational modes computed in the D band region, we have selected some of them based on the significance of their computed Raman activity, which is reported in Tables 3 and 4 normalized with respect to the strongest transition in the D band region. These data show that several D_i components, determined by deconvolution of the experimental features, can be associated with two or more vibrational modes (labeled as d_{ia} , d_{ib} , ...) that are computed at close wavenumbers. In the last column of Tables 3 and 4, we report the sum of the Raman activities of the transitions assigned to each individual D_i experimental component.

The Raman activity data reported in Tables 3 and 4 indicate that for both **C216** and **C222**, the D region of the spectrum is dominated by a few main components that show remarkable Raman intensities. For **C222**, we predict two comparably strong transitions (d_3 and d_5) and a weaker component at higher wavenumber (d_8). These three major components can be directly identified by visual inspection in the experimental spectrum ($\lambda_{\text{exc}} = 514$ nm) and correspond to the three sharp and strong peaks of the computed spectra reported in the bottom panel of Figure 5. As it was mentioned, the intensity pattern predicted by DFT shows some inaccuracies. The theoretical spectrum of **C222** is dominated by the d_3 and d_5 doublet with similar intensities, whereas in the experimental spectrum, the higher wavenumber feature of the doublet is remarkably stronger, probably because of a significant contribution by D_6 and D_7 , which are too weak in the spectrum computed by DFT.

The structured Raman spectrum of **C216** in the D region is characterized by three strong lines (D_3 , D_4 , and D_5) and a weaker line at higher wavenumber (D_8). Some inaccuracies in the predicted intensity pattern are evident also in this case. However, at least for the case of the

TABLE 3 C216: Analysis of the DFT predicted Raman spectrum in the D region and correspondence with the experimentally determined bands components (D_i)

| Symmetry species | Assignment (d_i component) | Expt. Raman shift (cm^{-1}) | Theo. Raman shift (scaled, cm^{-1}) | Theo. Raman shift (cm^{-1}) | Normalized Raman activity (to d_3) | Normalized Raman activity (to $d_{3a} + d_{3b}$) |
|----------------------------|-------------------------------|--|---|--|---------------------------------------|---|
| E_g | d_1 | 1221 | 1235 | 1260 | 1.81 | 1.63 |
| E_g | d_2 | 1254 | 1251 | 1277 | 5.27 | 4.76 |
| A_{1g} | d_{3a} | 1271 | 1265 | 1291 | 100.00 | 100.00 |
| E_g | d_{3b} | | 1271 | 1297 | 10.86 | |
| E_g | d_{4a} | 1298 | 1294 | 1320 | 8.50 | |
| E_g | d_{4b} | | 1298 | 1324 | 5.92 | 53.09 |
| A_{1g} | d_{4c} | | 1300 | 1327 | 44.44 | |
| E_g | d_{5a} | 1329 | 1317 | 1344 | 5.32 | |
| A_{1g} | d_{5b} | | 1319 | 1346 | 60.74 | 65.99 |
| E_g | d_{5c} | | 1323 | 1350 | 7.10 | |
| E_g | d_6 | 1349 | 1347 | 1374 | 2.79 | 2.52 |
| E_g | d_{7a} | 1364 | 1355 | 1383 | 2.29 | |
| A_{1g} | d_{7b} | | 1357 | 1385 | 7.46 | 13.59 |
| E_g | d_{7c} | | 1364 | 1392 | 5.32 | |
| E_g | d_{8a} | 1375 | 1370 | 1398 | 2.74 | 4.50 |
| E_g | d_{8b} | | 1372 | 1400 | 2.24 | |
| A_{1g} | d_9 | 1395 | 1432 | 1461 | 2.89 | 2.61 |

Note: Normalized Raman activities from prediction at 514 nm. Bold characters indicate very strong or strong transitions.

Abbreviation: DFT, density functional theory.

TABLE 4 C222: analysis of the DFT predicted Raman spectrum in the D region and correspondence with the experimentally determined bands components (D_i)

| Symmetry species | Assignment (d_i component) | Expt. Raman shift (cm^{-1}) | Theo. Raman shift (scaled, cm^{-1}) | Theo. Raman shift (cm^{-1}) | Normalized Raman activity (to d_3) | Normalized Raman activity (to d_3) |
|----------------------------|-------------------------------|--|---|--|---------------------------------------|---------------------------------------|
| E_g | d_1 | 1225 | 1238 | 1263 | 1.81 | 1.81 |
| A_{1g} | d_2 | 1240 | 1255 | 1281 | 0.24 | 0.24 |
| A_{1g} | d_3 | 1261 | 1266 | 1292 | 100.00 | 100.00 |
| A_{1g} | d_4 | 1273 | 1273 | 1299 | 3.29 | 3.29 |
| A_{1g} | d_5 | 1292 | 1292 | 1318 | 60.08 | 60.08 |
| E_g | d_6 | 1306 | 1298 | 1324 | 0.48 | 0.48 |
| E_g | d_{7a} | 1324 | 1317 | 1344 | 0.48 | 1.76 |
| A_{1g} | d_{7b} | | 1320 | 1347 | 1.29 | |
| A_{1g} | d_8 | 1357 | 1348 | 1376 | 15.63 | 15.63 |
| A_{1g} | d_{9a} | 1375 | 1366 | 1394 | 1.33 | 1.81 |
| A_{1g} | d_{9b} | | 1369 | 1397 | 0.48 | |
| A_{1g} | d_{10} | 1397 | 1395 | 1423 | 0.43 | 0.43 |

Note: Normalized Raman activities from prediction at 514 nm. Bold characters indicate very strong or strong transitions.

Abbreviation: DFT, density functional theory.

excitation at 458 nm, DFT calculations provide the correct intensity trend.

The analysis of the nuclear displacements (vibrational eigenvectors) computed by DFT can be used for drawing a close correlation between the Raman spectroscopy of NGs and that of graphene. Furthermore, it also provides information about spectral markers specifically related to the molecular structure. We report the graphical representation of the most representative eigenvectors of **C216** and **C222** in Figures 7 and 8, respectively.

The d_3 and d_5 eigenvectors of **C222** clearly describe the collective ring breathing vibrations of the Clar rings of the molecule (cf., for instance, with the chemical structure of Figure 1b). This nuclear displacement pattern is very similar to that of the phonon at K wave vector of graphene (see Figure 6b). The d_5 mode principally involves the central region of the molecule, whereas the d_3 mode shows the largest vibrational displacements for the rings at the molecular periphery. The d_3 mode also shows a remarkable contribution of CH wagging motions dynamically coupled with the CC stretching on the edges. Both d_3 and d_5 are collective modes spanning over the whole π -conjugated network of the molecule.

The d_8 mode of **C222** is peculiar because the ring breathing is well localized in the inner rings. Focusing on the central ring and on the six rings condensed on its edges, one can realize that this mode mimics the vibrational pattern of the D mode of a central coronene subunit, which of course cannot find any correspondence in the holey **C216**. This observation suggests that d_8 is a

characteristic feature of **C222**. We report in Figure 8 also the sketch of the normal modes assigned to the weak d_1 feature. These form a degenerate pair belonging to the E_g symmetry species, and it is described by two orthogonal vibrational patterns involving collective breathing vibrations of sequences of rings close to the edges.

The d_3 and d_4 modes of **C216** (Figure 7) display the characteristic nuclear displacement pattern found in the D-modes of NGs^[33] d_4 is more localized in the internal region of the circular crown, while mode d_3 has nuclear displacements, which are larger at the outer edge. **C216** shows a third remarkable and strong feature above 1300 cm^{-1} (d_5); this is still a collective breathing of the rings but also involves the CC stretching of the bonds forming the edge of the hole. For this reason, we can take d_5 as a nice Raman marker of the hole.

We note that the D_3 , D_4 , and D_5 triplet of **C216** (experimental wavenumbers: 1271 , 1298 , and 1329 cm^{-1}) overall shifts at higher wavenumbers with respect to the D_3 and D_5 doublet of **C222** (1261 and 1292 cm^{-1}). This is an expected feature of the Raman D lines of NGs (PAHs) of decreasing π conjugation/molecular size,^[34] as the hole in **C216** breaks π conjugation with respect to **C222**.

The details of the G Raman band of **C216** and **C222** are represented in Figure S1 (supporting information). The experimental spectra of both molecules show a single feature with a broad and asymmetric profile, which changes its shape with the laser excitation. The case of **C216** requires at least three components to properly fit the G band at different excitation energies. Two

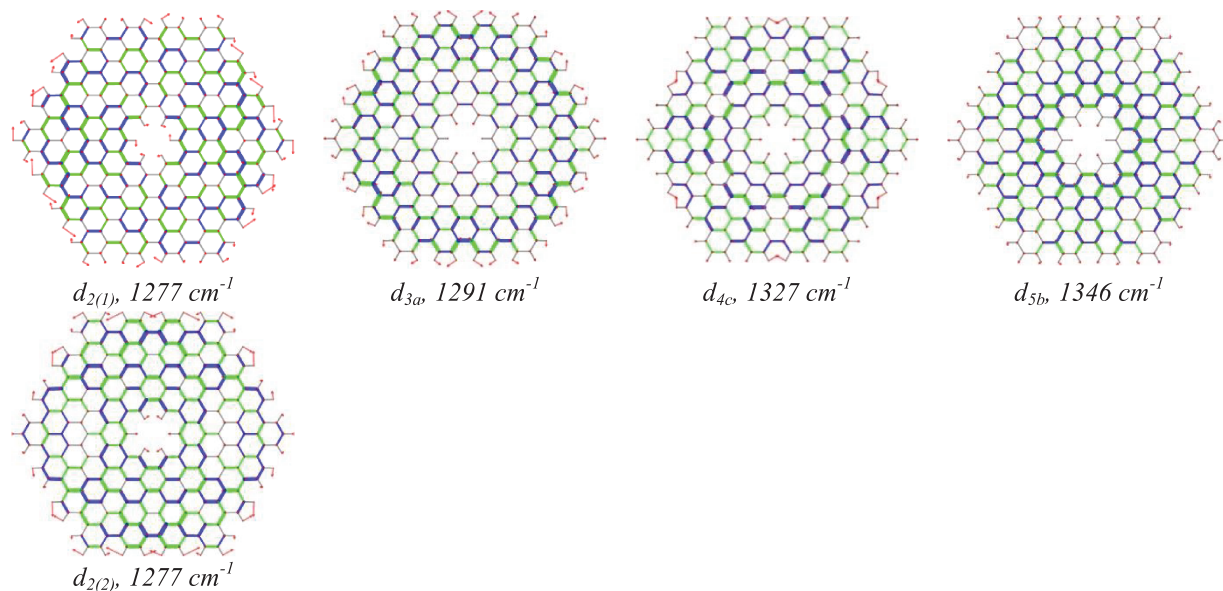


FIGURE 7 Representation of the normal modes of **C216** associated with the main experimental D band features. Red arrows represent displacement vectors; CC bonds are represented as green and blue lines of different thicknesses according to their relative stretching (shrinking)

components are enough for **C222**. Indeed, the G band of **C216** shows a more evident structure, with a marked shoulder on the lower wavenumber wing. DFT calculations predict several fairly close vibrational transitions that can be put in correspondence with the experimental features (G_i)—see Tables 5 and 6, and the bar plots reported in the bottom of each panel of Figure S1.

The relevant g_i modes with strongest Raman activity are represented in Figures 9 and 10, and they all show displacements patterns that are very similar to one of the degenerate components of the G mode of graphene (E_{2g} species—see Figure 6a).^[33] Modes g_{1b} (**C216**) and g_{1a} (**C222**) belong to E_g symmetry species and show the closest resemblance to the G mode of graphene. Very interestingly, based on DFT results, both experimental

features G_1 and G_2 of **C222** receive contributions from A_g modes: the intensity of the G_2 component is mostly ascribed to the two strong modes g_{2b} and g_{2c} (Table 6). For g_{2b} , the G-phonon pattern (Figure 6a) can be identified by looking at the radial displacements occurring at the six corners of **C222** (Figure 10). In g_{2c} , the G phonon pattern runs parallel to the six armchair edges of **C222**, following the molecular contour. The same pattern of g_{2b} of **C222** is also found for the totally-symmetric g_{3b} mode of **C216**, which corresponds to the strongest Raman transition in the G band. With respect to the collective g_{1a} mode of **C222**, the patterns of g_{1c} and g_2 (E_g symmetry) of **C216** are more localized.

As a final remark about the G band region, we observe that it is difficult to identify there a marker of the

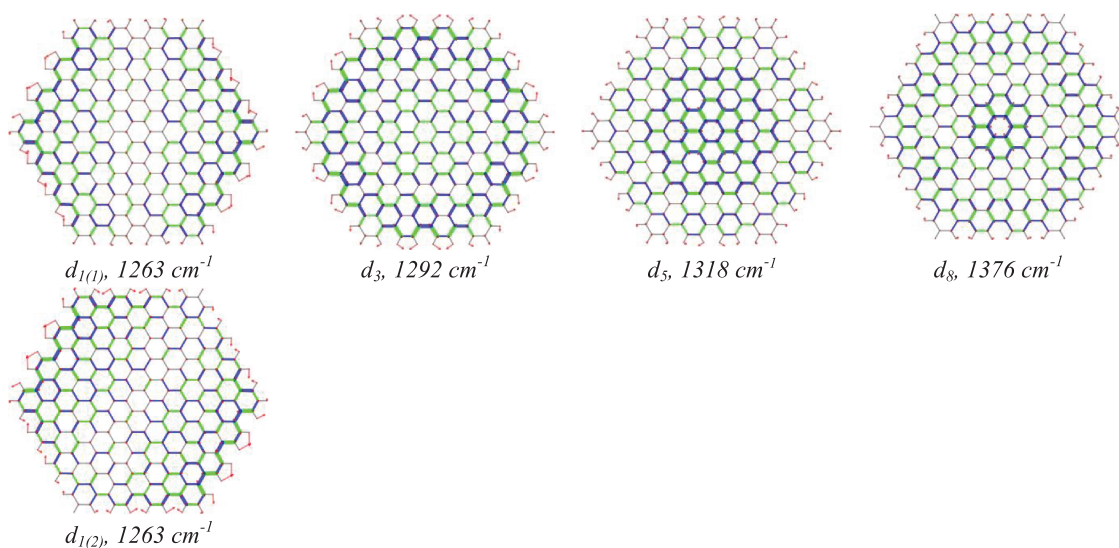


FIGURE 8 Representation of the normal modes of **C222** associated with the main experimental D band features. Red arrows represent displacement vectors; CC bonds are represented as green and blue lines of different thicknesses according to their relative stretching (shrinking)

TABLE 5 **C216**: Analysis of the DFT predicted Raman spectrum in the G region and correspondence with the experimentally determined bands components (G_i)

| Symmetry species | Assignment (g_i component) | Expt. Raman shift (cm^{-1}) | Theo. Raman shift (scaled, cm^{-1}) | Theo. Raman shift (cm^{-1}) | Normalized Raman activity (to g_{3b}) | Normalized Raman activity (to g_3) |
|------------------|-------------------------------|--|---|--|--|---------------------------------------|
| A_{1g} | g_{1a} | | 1593 | 1626 | 7.63 | 7.63 |
| E_g | g_{1b} | 1596 | 1600 | 1633 | 41.29 | 64.05 |
| E_g | g_{1c} | | 1603 | 1636 | 19.61 | |
| E_g | g_2 | 1612 | 1613 | 1646 | 98.52 | 92.09 |
| E_g | g_{3a} | | 1617 | 1650 | 6.99 | |
| A_{1g} | g_{3b} | 1618 | 1619 | 1652 | 100.00 | 100.00 |

Note: Normalized Raman activities from prediction at 514 nm. Bold characters indicate very strong transitions. Abbreviation: DFT, density functional theory.

TABLE 6 **C222**: analysis of the DFT predicted Raman spectrum in the G region and correspondence with the experimentally determined bands components (G_i)

| Symmetry species | Assignment (g_i component) | Expt. Raman shift (cm^{-1}) | Theo. Raman shift (scaled, cm^{-1}) | Theo. Raman shift (cm^{-1}) | Normalized Raman activity (to g_{1a}) | Normalized Raman activity (to g_2) |
|-------------------------|-------------------------------|--|---|--|--|---------------------------------------|
| E_{2g} | g_{1a} | 1595 | 1597 | 1630 | 100.00 | |
| A_g | g_{1b} | | 1600 | 1633 | 3.41 | 72.08 |
| E_{2g} | g_{1c} | | 1602 | 1635 | 1.36 | |
| E_{2g} | g_{2a} | | 1617 | 1650 | 1.63 | |
| A_g | g_{2b} | 1615 | 1617 | 1650 | 76.02 | 100.00 |
| A_g | g_{2c} | | 1619 | 1652 | 61.44 | |
| E_{2g} | g_{2d} | | 1619 | 1652 | 6.27 | |

Note: Normalized Raman activities from prediction at 514 nm. Bold characters indicate very strong transitions.

Abbreviation: DFT, density functional theory.

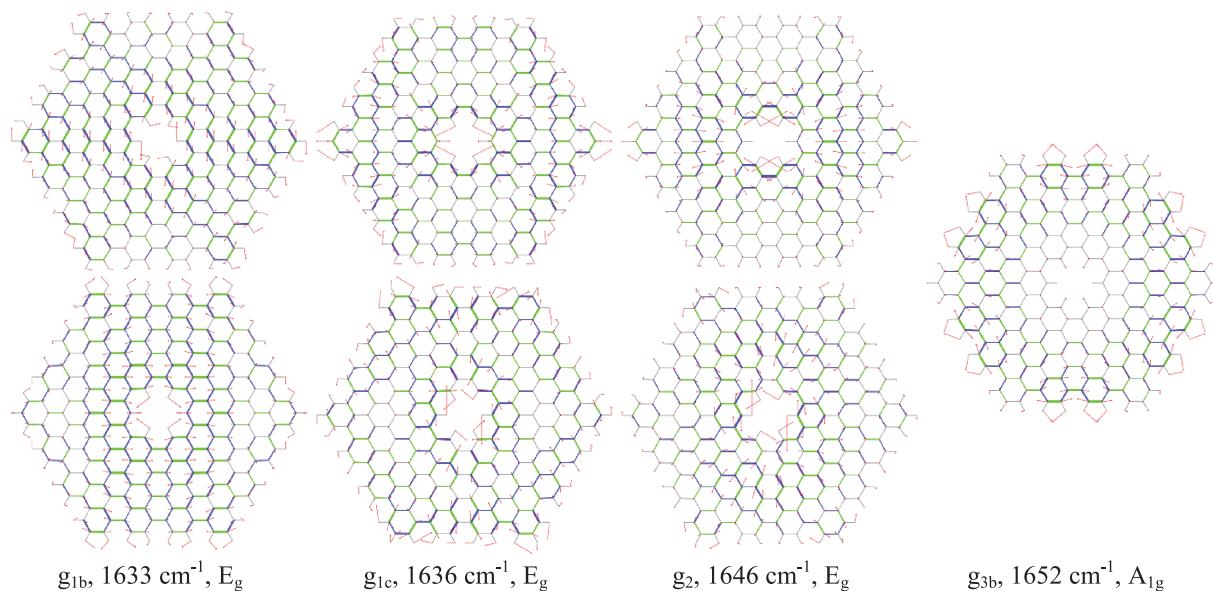


FIGURE 9 Sketch of the normal mode eigenvectors of **C216** associated with the main experimental G band features. Red arrows represent displacement vectors; CC bonds are represented as green and blue lines of different thicknesses according to their relative stretching (shrinking)

hole, even though the number of G_i components in **C216** is larger than in **C222**. Moreover, the G band features do not show any remarkable wavenumber shift in presence of the hole, at difference from the case of the D band.

3.2 | Low wavenumber region

The low-wavenumber region of the spectrum of **C216** has been recorded with 458, 514, and 633 nm excitations: thanks to the varying resonance conditions, the joint analysis of the spectra allows to clearly identify several

Raman transitions in this region (see Figure 11 and Table 7). In the bottom of Figure 11, we report for comparison also the Raman spectrum of **C222**, recorded with 458 nm (the most effective resonance condition).

C216 shows several collective deformation modes (A_1 , A_2 , and A_6). Features A_1 and A_2 are assigned to E_g modes that involve a shear-like deformation of the large hexagon in which **C216** can be inscribed (Figure 12). A_6 is assigned to a pair of modes at close wavenumbers that can be described as the breathing vibration of the hole. These two modes show a very similar displacement pattern involving the radial displacement of the carbon

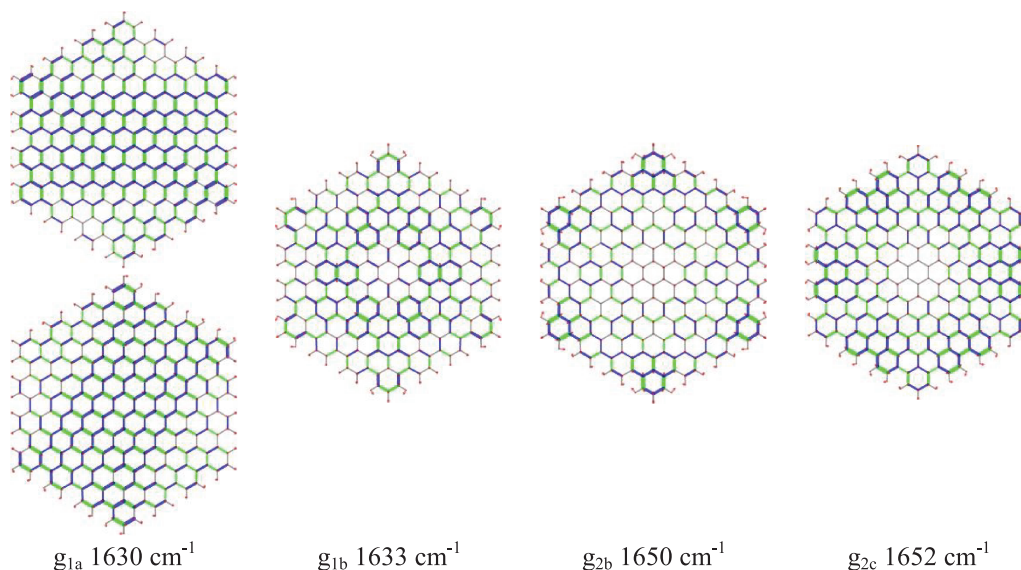


FIGURE 10 Sketch of the normal mode eigenvectors of **C222** associated with the main experimental G_1 and G_2 band features. Red arrows represent displacement vectors; CC bonds are represented as green and blue lines of different thicknesses according to their relative stretching (shrinking)

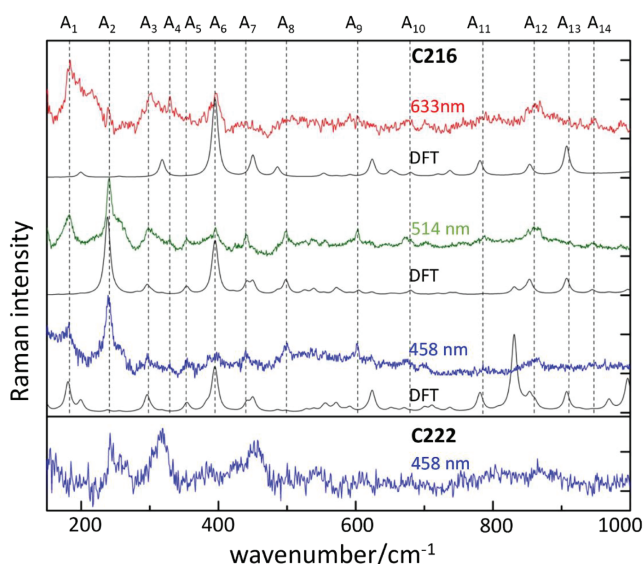


FIGURE 11 Low wavenumber region of the experimental Raman spectrum of **C216**, recorded with different laser excitations. Raman spectra computed by DFT at the same excitation wavelength are also shown. The bottom panel shows the experimental spectrum of the **C222**, recorded with 458-nm laser excitation

atoms on the edge of the hole (Figure 12). Resonance effects take place in the low-wavenumber region of the Raman spectrum, where the experimental spectrum is rich of signals. Consistently, Raman spectra simulated with DFT calculations are very sensitive to the selected excitation wavelength: for instance, the A_1 peak acquires

strong intensity with 458-nm excitation, and the A_2 peak with 514-nm excitation (Figure 11).

3.3 | High wavenumber region

Due to resonance Raman conditions, in NGs, it is possible to observe second-order Raman transitions,^[77] similar to defective graphite^[78] and graphene.^[47] As discussed in Maghsoumi et al.,^[77] for NGs such transitions involve two quanta, thus leading to 2D, D + G, and 2G bands.^[47,78]

In graphene and NGs,^[77] it is possible to observe second-order Raman transitions which involve two quanta, thus leading to 2D, D + G, and 2G bands. This is also the case of **C216**, for which we can observe such overtones and combination bands thanks to the resonance conditions that are expected for the 514 nm excitation (see Figure S2—supporting information). Remarkably, we observe not only two quanta Raman transitions but also three quanta Raman transitions assigned to 3D, 2D + G, 2G + D, and 3G overtone/combination bands (Figure 13). A survey of the Raman spectrum of **C216** excited with the 514-nm laser line in the region from 150 to 5000 cm^{-1} is shown in Figure 13, and the close comparison of the first-, second-, and third-order regions is shown in Figure 14.

Notably, the Raman intensity profiles in the two- and three-quanta transitions are reminiscent of the intensity pattern found in the first-order Raman spectrum (see Figure 14). This has been observed previously by

TABLE 7 List of observed and computed (unscaled) Raman features of C216 in the low-wavenumber region

| Feature # | Wavenumber (DFT) | Wavenumber (458 nm) | Wavenumber (514 nm) | Wavenumber (633 nm) |
|-----------------|---|---------------------|---------------------|---------------------|
| A ₁ | 184 (E _g) | 182 | 183 | 184 |
| A ₂ | 242 (E _g) | 239 | 241 | 239 |
| A ₃ | 301 (E _g) | 296 | 298 | 302 |
| A ₄ | 335 (E _g) | 329 | 329 | 329 |
| A ₅ | 359 (E _g) | 355 | 353 | 358 |
| A ₆ | 400, 403 (A _{1g} , A _{1g}) | 397 | 395 | 396 |
| A ₇ | 448 (E _g) | 440 | 440 | 441 |
| A ₈ | 506 (E _g) | 500 | 499 | 499 |
| A ₉ | 614 (E _g) | 602 | 603 | 603 |
| A ₁₀ | 691 (A _{1g}) | 676 | 676 | 677 |
| A ₁₁ | 798 (E _g) | 785 | 788 | 789 |
| A ₁₂ | 867 (A _{1g}) | 860 | 860 | 861 |
| A ₁₃ | 922 (A _{1g}) | - | 912 | - |
| A ₁₄ | 960 (E _g) | 947 | 947 | 947 |

Abbreviation: DFT, density functional theory.

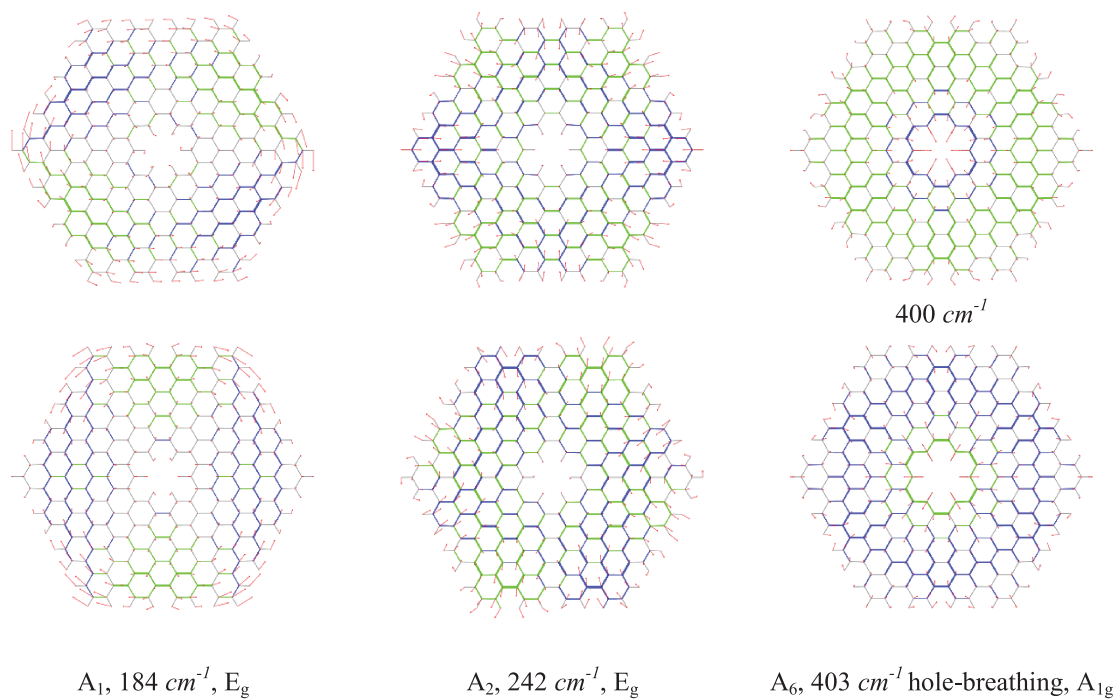


FIGURE 12 Sketch of the normal modes of C216 associated with the main experimental A band features. Red arrows represent displacement vectors; CC bonds are represented as green and blue lines of different thicknesses according to their relative stretching (shrinking)

Maghsoumi et al.^[77] and rationalized based on a theoretical description of the Raman cross section for overtones and combinations, which, under resonance conditions, leads to the following approximate relation:

$$I_{h+k} \approx I_h I_k \quad (1)$$

where I_h and I_k denote the Raman intensities of two first-order Raman transitions and I_{h+k} denotes the

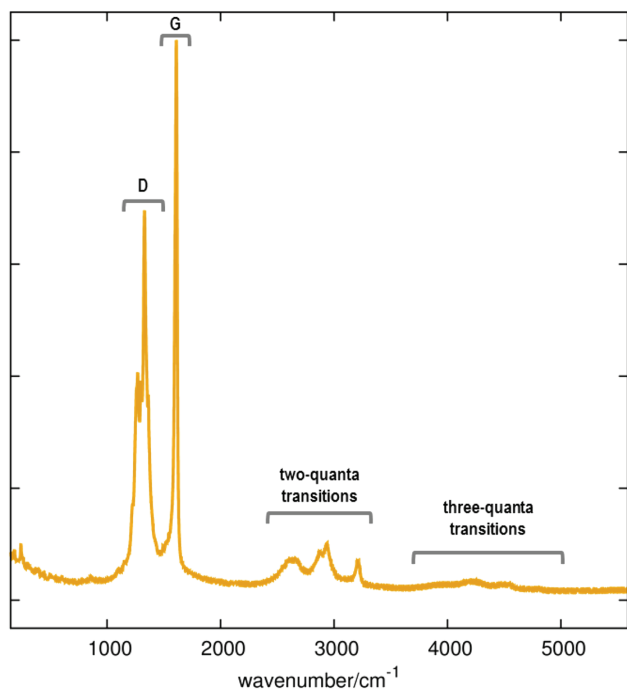


FIGURE 13 Raman spectrum of **C216** displayed over the fundamental ($150\text{--}1700\text{ cm}^{-1}$) and overtones/combinations regions ($2200\text{--}5000\text{ cm}^{-1}$). Two-quanta Raman transitions assigned to (2D, G + D, and 2G) are easily observed between 2200 and 3500 cm^{-1} and weaker three-quanta Raman transitions assigned to (3D, 2D + G, D + 2G, and 3G), which are observed above 3600 cm^{-1}

Raman intensity of the corresponding combination, with $h = k$ in the case of an overtone. This relationship justifies the experimental Raman data shown in Figure 14 and helps in assigning them straightforwardly. The position of the overtones of the G and D bands is close to the one expected from harmonic approximation. The structured shape of the D band leads to 2D and 3D features, which are progressively broader and less structured. This is due to the increasing number of possible combination transitions among those assigned to the several individual D_i components, the convolution of which gives rise to increasingly broad features. Moreover, starting from the same set of D_i components, there is a greater number of combinations corresponding to three quanta transitions, with respect to the two quanta ones. This allows understanding why the 3D region shows a less structured band than the 2D feature, as clearly observed in Figure 14. With the same approach, supported by Equation (1), it is also straightforward to justify the two features observed in the G+D band, which are due to the relatively sharp first-order G peak (G_i components rather close in wavenumber) combined with the several D_i components which form the structured D band.

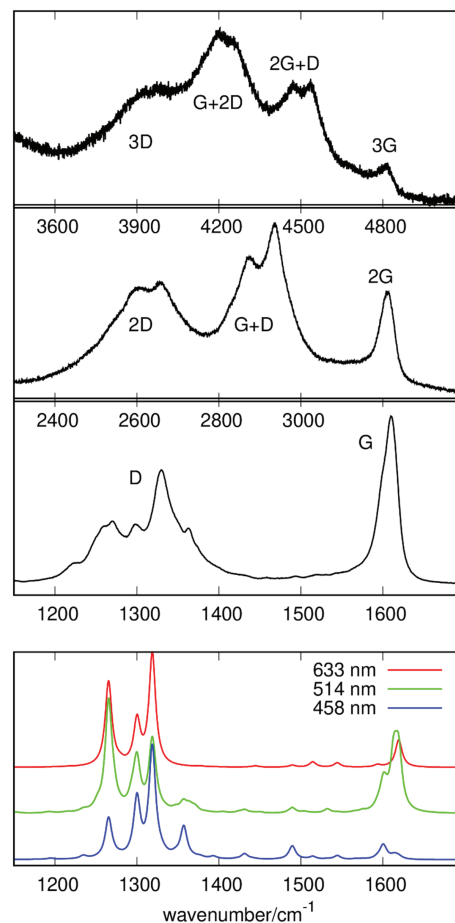


FIGURE 14 Raman spectrum of **C216** in the overtones and combination regions involving two and three quanta processes (recorded with 514-nm excitation). The first-order Raman spectrum is also displayed (bottom) to help assigning overtones and combinations based on the associated fundamentals. The bottom panel shows the simulated first-order Raman spectra based on DFT calculations of the Raman cross section for three selected excitation wavelengths

4 | CONCLUSIONS

The results discussed in this work are representative of the kind of information that can be obtained by Raman spectroscopy of NGs. We have investigated a relevant member of this class of compounds, namely, the holey NG **C216**, which is structurally related with **C222**.^[68] The assignment of the most notable experimental Raman features has been fostered by DFT calculations that allow to describe in detail the associated nuclear displacement patterns. The identification of such patterns allows to relate the given normal modes of the NGs to the G and D phonons of the parent graphene sheet, confined in different ways. Such a molecular approach has already been introduced for coronene and hexabenzocoronene,^[34] and finds its applicability also to the finite nanodomain of **C216**.

Through the analysis of the Raman spectra of **C216**, we have also found specific markers of the hole. Indeed, the presence of a hole in the graphene network does affect π conjugation, as evidenced by the higher wavenumber of the D band of **C216** compared with **C222**. Therefore, the hole effectively reduces the extent of π conjugation along the network of condensed aromatic rings. The presence of a hole in extended NGs such as **C216** is also a source of nonplanarity. This behavior bears similarities with the nonplanarity observed in many NGs upon chlorination at their edges.^[22,40]

Finally, thanks to good resonance Raman conditions, we have recorded and assigned well-resolved third-order Raman transitions, which were not observed before in NGs. It is believed that the present study can further support the key role of Raman spectroscopy for the precision synthesis and materials science of graphene structures.

5 | EXPERIMENTAL AND COMPUTATIONAL METHODS

Samples of **C216** and **C222** were synthesized as described in Beser et al. and Simpson et al.,^[32,68] respectively. The Raman spectra excited with the 488-nm laser line were recorded with a JASCO NRS-4100 Raman spectrometer coupled with a sapphire SF CDRH USB Laser (single-frequency optically pumped semiconductor laser).

All the other Raman spectra presented in this work were recorded with a Jobin-Yvon Labram HR800UV spectrometer, operated with different lasers, namely He-Cd laser (325 nm), Ar⁺ laser (457.9 and 514.5 nm), He-Ne laser (632.8 nm), and a high power solid-state diode laser (785 nm).

The laser power at the sample was always of the order of a few milliwatts to prevent laser-induced effects on the samples; care has been adopted to verify the reproducibility of the spectra. The samples were analyzed in the back-scattering geometry on glass slides by using the microscope with the 50X objective for all laser lines except the one at 325 nm, for which we used an ultraviolet (UV)-grade 15X objective. With the exception of the Raman spectra recorded with 325- and 488-nm excitations, the intensities of all the Raman spectra have been corrected with white light calibration.

The DFT calculations reported in this work have been carried out using the Gaussian code.^[79] We adopted the B3LYP functional and the 6-31G(d,p) basis set, which proved to be reliable for this class of molecules.^[68] Raman intensities have been computed from the frequency-dependent molecular polarizability derivatives at selected incident light wavelengths, as implemented in

Gaussian09.^[79] This approach may yield useful information in the case of pre-resonance/near resonance Raman conditions.

A set of post-processing programs developed at Politecnico di Milano has been used to generate the representation of the vibrational normal modes and simulate the Raman spectra from the results of DFT calculations.

ACKNOWLEDGEMENTS

K. M. acknowledges the generous support of his Emeritus group by the Max Planck Society. A. N. acknowledges the financial support by the Max Planck Society. C. C. and M. T. acknowledge funding by the Italian Ministry of Education, Universities and Research (MIUR) through the PRIN 2017 program (Project No. 2017PJ5XXX "MAGIC DUST"). Open Access Funding provided by Politecnico di Milano within the CRUI-CARE Agreement.

DATA AVAILABILITY STATEMENT

Data available on request from the authors


ORCID

Ali Maghsoumi  <https://orcid.org/0000-0002-8114-7383>

Xinliang Feng  <https://orcid.org/0000-0003-3885-2703>

Akimitsu Narita  <https://orcid.org/0000-0002-3625-522X>

Klaus Müllen  <https://orcid.org/0000-0001-6630-8786>

Chiara Castiglioni  <https://orcid.org/0000-0002-6945-9157>

Matteo Tommasini  <https://orcid.org/0000-0002-7917-426X>

REFERENCES

- [1] X.-Y. Wang, X. Yao, K. Müllen, *Sci. China Chem.* **2019**, *62*, 1099.
- [2] E. Clar, W. Schmidt, *Tetrahedron* **1979**, *35*(22), 2673.
- [3] S. E. Stein, R. L. Brown, *J. Am. Chem. Soc.* **1987**, *109*, 3721.
- [4] A. Pathak, S. Rastogi, *Spectrochim. Acta A* **2007**, *67*, 898.
- [5] R. Rieger, K. Müllen, *J. Phys. Org. Chem.* **2010**, *23*, 315.
- [6] D. Setiawan, E. Kraka, D. Cremer, *J. Org. Chem.* **2016**, *81*(20), 9669.
- [7] I. R. Marquez, S. Castro-Fernandez, A. Millan, A. G. Campana, *Chem. Commun.* **2018**, *54*, 6705.
- [8] I. Pozo, E. Guitian, D. Perez, D. Peña, *Acc. Chem. Res.* **2019**, *52*, 2472.
- [9] H. Ito, Y. Segawa, K. Murakami, K. Itami, *J. Am. Chem. Soc.* **2019**, *141*, 3.
- [10] W. Chen, F. Yu, Q. Xu, G. Zhou, Q. Zhang, *Adv. Sci.* **2020**, *7* (12), 1903766.
- [11] J. A. McGuire, *Phys. Status Solidi RRL* **2016**, *10*, 91.
- [12] K. P. Loh, S. W. Tong, J. Wu, *J. Am. Chem. Soc.* **2016**, *138*, 1095.
- [13] V. Bonal, R. Muñoz-Mármol, F. Gordillo Gámez, M. Morales-Vidal, J. M. Villalvilla, P. G. Boj, J. A. Quintana, Y.

- Gu, J. Wu, J. Casado, M. A. Díaz-García, *Nat. Commun.* **2019**, *10*(1), 3327.
- [14] A. Narita, X.-Y. Wang, X. Feng, K. Müllen, *Chem. Soc. Rev.* **2015**, *44*(18), 6616.
- [15] M. Stępień, E. Gońka, M. Żyła, N. Sprutta, *Chem. Rev.* **2017**, *117*(4), 3479.
- [16] X.-Y. Wang, X. Yao, A. Narita, K. Müllen, *Acc. Chem. Res.* **2019**, *52*(9), 2491.
- [17] I. Diez-Perez, Z. Li, J. Hihath, J. Li, C. Zhang, X. Yang, L. Zang, Y. Dai, X. Feng, K. Müllen, N. Tao, *Nat. Commun.* **2010**, *1*, 31.
- [18] B. Limburg, J. O. Thomas, G. Holloway, H. Sadeghi, S. Sangtarash, I. C.-Y. Hou, J. Cremers, A. Narita, K. Müllen, C. J. Lambert, G. A. D. Briggs, J. A. Mol, H. L. Anderson, *Adv. Funct. Mater.* **2018**, *28*, 1803629.
- [19] J. Wu, W. Pisula, K. Müllen, *Chem. Rev.* **2007**, *107*, 718.
- [20] X. Feng, M. Liu, W. Pisula, M. Takase, J. Li, K. Müllen, *Adv. Mater.* **2008**, *20*, 2684.
- [21] Y. Morita, S. Suzuki, K. Sato, T. Takui, *Nat. Chem.* **2011**, *3*, 197.
- [22] Y.-Z. Tan, B. Yang, K. Parvez, A. Narita, S. Osella, D. Beljonne, X. Feng, K. Müllen, *Nat. Commun.* **2013**, *4*, 2646.
- [23] Y. Dai, Z. Li, J. Yang, *ChemPhysChem* **2015**, *16*, 2783.
- [24] S. Ito, M. Wehmeier, J. D. Brand, C. Kübel, R. Epsch, J. P. Rabe, K. Müllen, *Chem. A Eur. J.* **2000**, *6*, 4327.
- [25] T. Böhme, C. D. Simpson, K. Müllen, J. P. Rabe, *Chem. A Eur. J.* **2007**, *13*, 7349.
- [26] Ž. Tomović, M. D. Watson, K. Müllen, *Angew. Chem. Int. Ed.* **2004**, *43*, 755.
- [27] J. P. Schmidtke, R. H. Friend, M. Kastler, K. Müllen, *J. Chem. Phys.* **2006**, *124*, 174704.
- [28] S. Laschat, A. Baro, N. Steinke, F. Giesselmann, C. Hägele, G. Scalia, R. Judele, E. Kapatsina, S. Sauer, A. Schreivogel, M. Tosoni, *Angew. Chem. Int. Ed.* **2007**, *46*, 4832.
- [29] W. Pisula, X. Feng, K. Müllen, *Chem. Mater.* **2011**, *23*, 554.
- [30] X.-Y. Wang, A. Narita, K. Müllen, *Nat. Rev. Chem.* **2017**, *2*, 0100.
- [31] J. Liu, X. Feng, *Angew. Chem. Int. Ed.* **2020**, *59*, 23386.
- [32] C. D. Simpson, J. D. Brand, A. J. Berresheim, L. Przybilla, H. J. Räder, K. Müllen, *Chem. A Eur. J.* **2002**, *8*, 1424.
- [33] C. Castiglioni, M. Tommasini, G. Zerbi, *Phil. Trans. R. Soc. Lond. A* **2004**, *362*, 2425.
- [34] C. Mapelli, C. Castiglioni, G. Zerbi, K. Müllen, *Phys. Rev. B* **1999**, *60*, 12710.
- [35] C. Castiglioni, C. Mapelli, F. Negri, G. Zerbi, *J. Chem. Phys.* **2001**, *114*, 963.
- [36] A. Narita, Z. Chen, Q. Chen, K. Müllen, *Chem. Sci.* **2019**, *10*, 964.
- [37] A. Jolly, D. Miao, M. Daigle, J.-F. Morin, *Angew. Chem. Int. Ed.* **2020**, *59*, 4624.
- [38] K.-Y. Yoon, G. Dong, *Mater. Chem. Front.* **2020**, *4*, 29.
- [39] D. Jariwala, A. Srivastava, P. M. J. J. Ajayan, *Nanosci. Nanotechnol.* **2011**, *11*, 6621.
- [40] A. Maghsoumi, A. Narita, R. Dong, X. Feng, C. Castiglioni, K. Müllen, M. Tommasini, *Phys. Chem. Chem. Phys.* **2016**, *18*, 11869.
- [41] W. Yang, A. Lucotti, M. Tommasini, W. A. Chalifoux, *J. Am. Chem. Soc.* **2016**, *138*(29), 9137.
- [42] X.-Y. Wang, T. Dienel, M. Di Giovannantonio, G. B. Barin, N. Kharche, O. Deniz, J. I. Urgel, R. Widmer, S. Stolz, L. H. De Lima, M. Muntwiler, M. Tommasini, V. Meunier, P. Ruffieux, X. Feng, R. Fasel, K. Müllen, A. Narita, *J. Am. Chem. Soc.* **2017**, *139*(13), 4671.
- [43] W. Yang, G. Longhi, S. Abbate, A. Lucotti, M. Tommasini, C. Villani, V. J. Catalano, A. O. Lykhin, S. A. Varganov, W. A. Chalifoux, *J. Am. Chem. Soc.* **2017**, *139*, 13102.
- [44] M. Daigle, D. Miao, A. Lucotti, M. Tommasini, J. F. Morin, *Angew. Chem. Int. Ed.* **2017**, *56*(22), 6213.
- [45] X.-Y. Wang, J. I. Urgel, G. B. Barin, K. Eimre, M. Di Giovannantonio, A. Milani, M. Tommasini, C. A. Pignedoli, P. Ruffieux, X. Feng, K. Müllen, A. Narita, *J. Am. Chem. Soc.* **2018**, *140*, 9104.
- [46] T. Dumsloff, Y. Gu, G. M. Paternò, Z. Qiu, A. Maghsoumi, M. Tommasini, X. Feng, F. Scotognella, A. Narita, K. Müllen, *Chem. Sci.* **2020**, *11*, 12816.
- [47] A. Ferrari, D. Basko, *Nature Nanotech* **2013**, *8*, 235.
- [48] E. Di Donato, M. Tommasini, G. Fustella, L. Brambilla, C. Castiglioni, G. Zerbi, C. D. Simpson, K. Müllen, F. Negri, *Chem. Phys.* **2004**, *301*, 81.
- [49] M. Tommasini, A. Lucotti, M. Alfè, A. Ciajolo, G. Zerbi, *Spectrochim. Acta A Mol. Biomol. Spectrosc.* **2016**, *152*, 134.
- [50] Q. Chen, L. Brambilla, L. Daukiya, K. S. Mali, S. De Feyter, M. Tommasini, K. Müllen, A. Narita, *Angew. Chem. Int. Ed.* **2018**, *57*(35), 11233.
- [51] H. Miyoshi, S. Nobusue, A. Shimizu, Y. Tobe, *Chem. Soc. Rev.* **2015**, *44*, 6560.
- [52] J. C. Buttrick, B. T. King, *Chem. Soc. Rev.* **2017**, *46*, 7.
- [53] H. A. Staab, F. Diederich, *Chem. Ber.* **1983**, *116*, 3487.
- [54] B. Kumar, R. L. Viboh, M. C. Bonifacio, W. B. Thompson, J. C. Buttrick, B. C. Westlake, S. Kim, R. W. Zoellner, S. A. Varganov, P. Mörschel, J. Teteruk, M. U. Schmidt, B. T. King, *Angew. Chem. Int. Ed.* **2012**, *51*, 12795.
- [55] N. Nishina, T. Mutai, J.-i. Aihara, *J. Phys. Chem. A* **2016**, *120*(15), 2431.
- [56] M. A. Majewski, Y. Hong, T. Lis, J. Gregoliński, P. J. Chmielewski, J. Cybińska, D. Kim, M. Stępień, *Angew. Chem. Int. Ed.* **2016**, *55*(45), 14072.
- [57] I. Pozo, Z. Majzik, N. Pavliček, M. Melle-Franco, E. Guitián, D. Peña, L. Gross, D. Pérez, *J. Am. Chem. Soc.* **2019**, *141*(39), 15488.
- [58] Q. Fan, D. Martin-Jimenez, S. Werner, D. Ebeling, T. Koehler, T. Vollgraff, J. Sundermeyer, W. Hieringer, A. Schirmeisen, J. M. Gottfried, *Am. Chem. Soc.* **2020**, *142*(2), 894.
- [59] H. Hou, X.-J. Zhao, C. Tang, Y.-Y. Ju, Z.-Y. Deng, X.-R. Wang, L.-B. Feng, D.-H. Lin, X. Hou, A. Narita, K. Müllen, Y.-Z. Tan, *Nat. Commun.* **2020**, *11*, 3976.
- [60] M. Di Giovannantonio, X. Yao, K. Eimre, J. I. Urgel, P. Ruffieux, C. A. Pignedoli, K. Müllen, R. Fasel, A. Narita, *J. Am. Chem. Soc.* **2020**, *142*(28), 12046.
- [61] X.-J. Zhao, H. Hou, P.-P. Ding, Z.-Y. Deng, Y.-Y. Ju, S. H. Liu, Y.-M. Liu, C. Tang, L.-B. Feng, Y.-Z. Tan, *Sci. Adv.* **2020**, *6*, eaay8541.
- [62] J. Bai, X. Zhong, S. Jiang, Y. Huang, X. Duan, *Nat. Nanotechnol.* **2010**, *5*, 190.
- [63] X. Liang, Y.-S. Jung, S. Wu, A. Ismach, D. L. Olynick, S. Cabrini, J. Bokor, *Nano Lett.* **2010**, *10*, 2454.

- [64] D. Jariwala, A. Srivastava, P. M. Ajayan, *J. Nanosci. Nanotechnol.* **2011**, *11*, 6621.
- [65] Z. Zeng, X. Huang, Z. Yin, H. Li, Y. Chen, H. Li, Q. Zhang, J. Ma, F. Boey, H. Zhang, *Adv. Mater.* **2012**, *24*, 4138.
- [66] M. Wang, L. Fu, L. Gan, C. Zhang, M. Rümmele, A. Bachmatiuk, K. Huang, Y. Fang, Z. Liu, *Sci. Rep.* **2013**, *3*, 1238.
- [67] A. W. Robertson, G.-D. Lee, K. He, C. Gong, Q. Chen, E. Yoon, A. I. Kirkland, J. H. Warner, *ACS Nano* **2015**, *9*(12), 11599.
- [68] U. Beser, M. Kastler, A. Maghsoumi, M. Wagner, C. Castiglioni, M. Tommasini, A. Narita, X. Feng, K. Müllen, *J. Am. Chem. Soc.* **2015**, *138*(13), 4322.
- [69] Y. Liu, W. Liu, J. Hou, Y. Dai, J. Yang, *Carbon* **2018**, *135*, 112.
- [70] E. Clar, *Aromatic Sextet*, John Wiley and Sons, Ltd, London, UK **1972**.
- [71] F. Negri, E. Di Donato, M. Tommasini, C. Castiglioni, G. Zerbi, K. Müllen, *J. Chem. Phys.* **2004**, *120*, 11889.
- [72] M. G. Schwab, A. Narita, S. Osella, Y. Hu, A. Maghsoumi, A. Mavrinsky, W. Pisula, C. Castiglioni, M. Tommasini, D. Beljonne, X. Feng, K. Müllen, *Chem. Asian J.* **2015**, *10*, 2134.
- [73] C. Thomsen, S. Reich, *Phys. Rev. Letters* **2000**, *85*, 5214.
- [74] C. Castiglioni, F. Negri, M. Rigoglio, G. Zerbi, *J. Chem. Phys.* **2001**, *115*, 3769.
- [75] A. Baiardi, J. Bloino, V. Barone, *J. Chem. Phys.* **2014**, *141*(11), 14108.
- [76] A. Baiardi, J. Bloino, V. Barone, *J. Chem. Theory Comput.* **2015**, *11*, 3267.
- [77] A. Maghsoumi, L. Brambilla, C. Castiglioni, K. Müllen, M. Tommasini, *J. Raman Spectrosc.* **2015**, *46*, 757.
- [78] M. Bonelli, A. Miotello, P. M. Ossi, A. Pessi, S. Gialanella, *Phys. Rev. B* **1999**, *59*, 13513.
- [79] M. J. Frisch, G. W. Trucks, H. B. Schlegel, G. E. Scuseria, M. A. Robb, J. R. Cheeseman, G. Scalmani, V. Barone, B. Mennucci, G. A. Petersson, H. Nakatsuji, M. Caricato, X. Li, H. P. Hratchian, A. F. Izmaylov, J. Bloino, G. Zheng, J. L. Sonnenberg, M. Hada, M. Ehara, K. Toyota, R. Fukuda, J. Hasegawa, M. Ishida, T. Nakajima, Y. Honda, O. Kitao, H. Nakai, T. Vreven, J. A. Montgomery Jr., J. E. Peralta, F. Ogliaro, M. Bearpark, J. J. Heyd, E. Brothers, K. N. Kudin, V. N. Staroverov, R. Kobayashi, J. Normand, K. Raghavachari, A. Rendell, J. C. Burant, S. S. Iyengar, J. Tomasi, M. Cossi, N. Rega, J. M. Millam, M. Klene, J. E. Knox, J. B. Cross, V. Bakken, C. Adamo, J. Jaramillo, R. Gomperts, R. E. Stratmann, O. Yazyev, A. J. Austin, R. Cammi, C. Pomelli, J. W. Ochterski, R. L. Martin, K. Morokuma, V. G. Zakrzewski, G. A. Voth, P. Salvador, J. J. Dannenberg, S. Dapprich, A. D. Daniels, Ö. Farkas, J. B. Foresman, J. V. Ortiz, J. Cioslowski, D. J. Fox, *Gaussian 09, Revision D.01*, Gaussian Inc., Wallingford CT **2009**.

SUPPORTING INFORMATION

Additional supporting information may be found online in the Supporting Information section at the end of this article.

How to cite this article: A. Maghsoumi, U. Beser, X. Feng, A. Narita, K. Müllen, C. Castiglioni, M. Tommasini, *J Raman Spectrosc* **2021**, *52*(12), 2301. <https://doi.org/10.1002/jrs.6189>